Solid Freeform Fabrication 2024: Proceedings of the 35th Annual International Solid Freeform Fabrication Symposium – An Additive Manufacturing Conference
Reviewed Paper

Investigating the Effect of Workpiece Shape on Thermal History and Coating Properties in High-speed Coatings using Laser Directed Energy Deposition

S. Takemura*, T. Mori†, Y. Hirono†, Y. Kakinuma*

*Department of System Desing Engineering, Keio University, Kohoku-ku, Yokohama, Kanagawa, Japan, 223-8522
†DMG MORI CO., LTD., Shiomi, Koto-ku, Tokyo, Japan, 135-0052

Abstract

Directed Energy Deposition (DED) can be used for metal coating as well as parts fabrication because it can supply powder and laser on the part surface freely. As for high-speed coating using DED, it has advantages such as high efficiency and reduced heat-affected zone. However, because of rapid heat input and cooling, it is considered that the thermal history of the coating layer becomes more sensitive to the coated workpiece shape, which can affect the coating properties. In this research, the effect of workpiece shape on thermal history during high-speed coating using DED is numerically analyzed. A thermal simulation of rotational coating is developed, where elements are added and the heat input area is moved according to laser scanning and workpiece rotation. Additionally, experiments are conducted to investigate the relationship between thermal history and coating quality and hardness. In this study, solid and hollow cylinders are selected as workpieces.

1. Introduction

Metal additive manufacturing (AM) has grown in recent years and significantly impacted various industries, for example, aviation, automotive, and medical industries[1,2]. Metal AM involves several types of process modes, for example, Powder Bed Fusion (PBF), Directed Energy Deposition (DED), Binder Jetting (BJ), and Material Extrusion (ME). In one of them, the DED process, the cladding layer is fabricated by supplying powders and melting and solidifying them with a heat source, such as a laser or electron beam as shown in **Figure 1**. DED is mainly used to fabricate parts with a near-net shape in the early stage[3]. However, DED is suitable not only for manufacturing parts but also for coatings that add material to existing parts, due to its material addition process. Moreover, in terms of the high-speed coating using DED, it has advantages such as high efficiency and lower heat affect zone (HAZ) of the substrate. However, in the metal AM process, metal materials are melted and solidified, rapidly and repeatedly. Furthermore, the rapid temperature deviation is repeated during the short term in the high-speed coating using DED, and their thermal history has a significant effect on the cladding layer's microstructure, properties, and quality[4]. For these reasons, investigating the thermal history during the high-speed coating using DED is important to analyze the cladding layer's properties as well as to optimize the process parameters.

To analyze the thermal history of metal AM, many studies using numerical simulation have been conducted with various processes and materials[5–10]. However, most simulations are developed for investigating the thin-wall or block-shape deposit with conventional speed, not for the high-speed coating on the substrate surface. Lv et. al[11] have developed the temperature field simulation of the extreme high-speed laser cladding (EHLA) process on a cylindrical substrate. In

their study, the simulated HAZ depth agreed well with the experimental results, but the simulation domain was relatively small with a diameter of 12 mm and a length of 12 mm, and thermal history was not analyzed in detail. Additionally, in the coating, the distance between the cladding points and the substrate is much closer throughout the entire process than in parts manufacturing, such as thin-wall or block-shape deposition. It means that the cladding layer is easily cooled by the workpiece with a large heat capacity. However, as the coating progresses, the heat accumulates in the workpiece, which is considered to affect the thermal history of the cladding layer, and consequently change the microstructure and mechanical properties.

In this research, the effect of workpiece shape on thermal history during high-speed coating using DED was analyzed based on the three-dimensional transient thermal analysis using the finite element (FE) simulation. Firstly, the heat-input and element-addition models were examined to simulate the temperature distribution in a simple way based on the observation and analysis of experimental results. Next, thermal simulations of the rotational coating were performed assuming solid and hollow cylinders as workpieces. In this simulation, the cylindric workpieces were converted to rectangular bodies to implement the elements additions considering overlap and reduce the computational cost. Moreover, the coating experiments were conducted to investigate the effect of workpiece shape and thermal history on the coating properties.

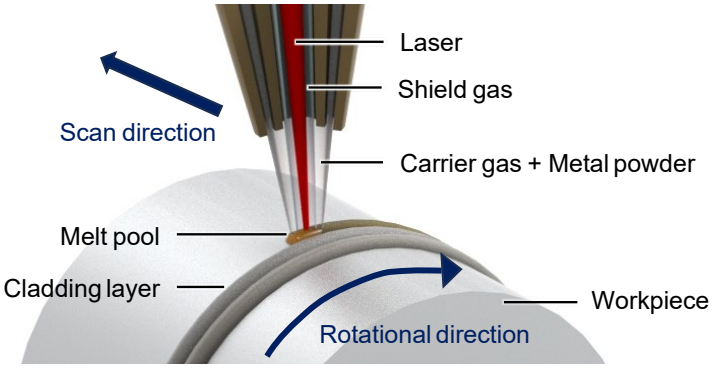

Figure 1 Schematics of rotational coating using DED

2. Numerical Modelling

The three-dimensional transient thermal analysis has been conducted using the commercial finite element simulation software ANSYS Parametric Design Language (APDL). In the numerical model of DED, the element birth and death feature[12] was adapted to simulate that the cladding material is supplied and added to the substrate continuously. In the element birth and death feature, the added elements are created at the start of the analysis, but they are deactivated and do not affect the analysis until the laser passes over them. In this study, the coating of tool steel Ferro55 on a stainless steel SUS304 workpiece was assumed. Since some physical properties of Ferro55 are not available, the coating material's physical properties were decided based on those of AISI H13 comparable to Ferro55[13]. As for the substrate, the physical properties of SUS304 were used.

2.1. Governing Equation and boundary conditions

The transient temperature field was obtained by solving the heat conduction equation defined as Eq.(1)

$$\frac{\partial}{\partial} = \frac{\partial}{\partial} + \frac{\partial}{\partial} + \frac{\partial}{\partial} + \tag{1}$$

where is the material density, is the specific heat capacity, is the temperature, is the thermal conductivity, and is the heat generated per unit volume.

As the boundary conditions, the heat convection and heat radiation were defined as Eq.(2), (3)

$$= \quad (\qquad) \tag{2}$$

$$= \quad (\qquad) \tag{3}$$

where is the coefficient for heat convection, is the Stefan–Boltzmann constant and is the emissivity.

In the AM system used in this study, the laser beam shape is top hat[14]. So, the laser beam was modeled as a uniform heat flux supplied within the laser spot of 3 mm diameter in this simulation, and heat flux was defined as Eq.(4).

$$= \frac{\qquad}{\qquad} \tag{4}$$

where is the laser power, is the absorption rate, and is the laser spot diameter.

2.2. FE Model Geometry and Mesh

To implement the elements additions considering overlap and reduce the computational cost, the half of cylindric workpieces were converted to rectangular bodies as shown in **Fig.2**. Although the rotating coating is not exactly a symmetric model, we attempted to simplify it by modeling only half of the workpiece, since the coating temperature drops rapidly due to the larger heat capacity of the workpiece compared to the coating layer and the fast rotational speed. In a solid cylinder, rectangular height was decided so that the cross-sectional area would be the same as the original solid cylinder (**Fig.2** (up)). A hollow cylinder's height was equal to the original hollow cylinder's thickness (**Fig.2** (down)). The details of geometry and mesh in this simulation are shown in **Fig.3** and dimensions of FE models are summarized in **Table 1**.

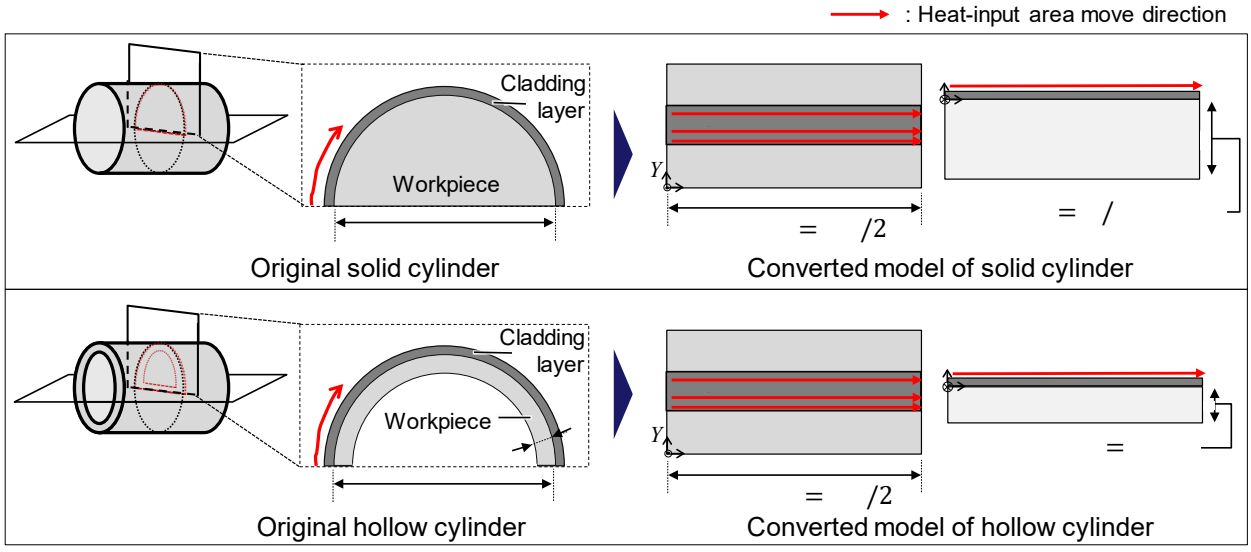

Figure 2 Conversion of workpiece geometry for simulation,
(up) solid cylinder model, (down) hollow cylinder model.

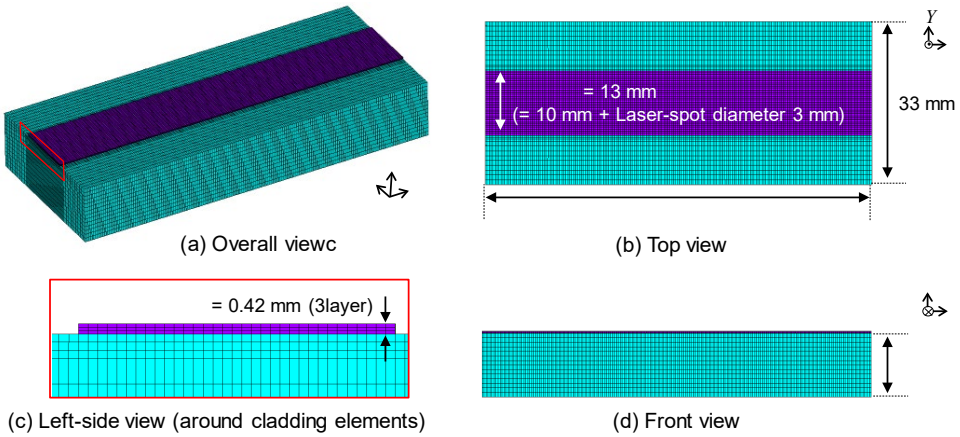

Figure 3 FE model geometry and mesh,
(a) overall view, (b) top view, (c) left-side view around cladding elements and (d) front view.

Table 1 Dimensions of FE models

Original dimensions (Unit: mm)	Solid	Hollow
Diameter	50	
Thickness	-	4.6
Converted dimensions (Unit: mm)	Solid	Hollow
Width	78.54	
	33	
Height	12.5	4.6
Number of model divisions	2	

The heat convection and radiation were applied to the outer surface of the active element where the Z-positive direction is normal. Other surfaces parallel to the YZ and ZX planes were assumed to be adiabatic.

2.3. Examination of the heat-input and element-addition model

In this study, heat-input and element-addition models suitable for high-speed coating using DED were examined to simulate the temperature distribution in a simple way. In studies about the thermal analysis of DED, several methods to model the heat source are used, and many studies have adapted the volumetric heat source, for example, Goldak's Gaussian ellipsoid model[5,6,15,16], the conical Gaussian cone model[17,18]. Those methods can take account of the three-dimensional laser profile, however, they have many parameters that are determined empirically, such as laser penetration depth[19]. Moreover, the HAZ in the high-speed coating is much thinner than conventional DED. So, a much finer mesh would be required to represent the laser profile shape in the depth direction, making simulations time-consuming. For these reasons, the surface heat source used in several research[7,20,21] was adapted in this study (Heat source distribution was uniform in this study.). However, in the high-speed coating, the laser irradiates for a very short time and, there are overlaps at a certain point in a short time, unlike general DEDs. Hence, generating the entire height of the coating layer at a time and adding a heat source to its surface within the melt pool range would not reproduce the temperature distribution in the depth direction. Therefore, in this study, 3 types of heat-input and element-addition models were created

as shown in **Fig.4**, and the temperature of the external surface of the melt pool and the interface between the base metal and the cladding layer immediately below it was compared for these models.

- In Type 1, the element-activated area is within the melt pool diameter (= 3 mm), and the entire height of one layer in that area is activated. As for the heat input area, it is the external top surface with a diameter of 3 mm, the same as the element-activated area. Therefore, once the melt pool has passed, no elements are produced at that location, only heat input to the surface in subsequent rounds.
- In Type 2, the element-activated area and heat input area are the same as in Type 1, but only elements as high as one mesh layer from the existing surface are activated. In this case, within the same round, an element at the same point (on the XY plane) is activated only once, and another element one level above the same point is activated in the next round.
- In Type 3, the heat input area is the same as in Type 1 and 2, but the element-activated area is within the diameter of 2 mm. The diameter of 2 mm was determined according to a preliminary experiment. By observation of the cross-sectional area of the cladding layer, it was found that the width of the deposit was smaller than the laser diameter in the high-speed coating, and it would be because the laser was moving too fast and not sufficiently heated the substrate to form a melt pool of the same size as the spot diameter. The method of element activation in the height direction is the same as Type 2.

To examine the 3 models, the thermal simulations for 10 seconds were conducted with laser power 2100 W, laser rotational speed 34.6 min^{-1}, and scan speed 20 mm/min, the same as the preliminary experiment. For this simulation, a 1/4 converted solid FE model was used.

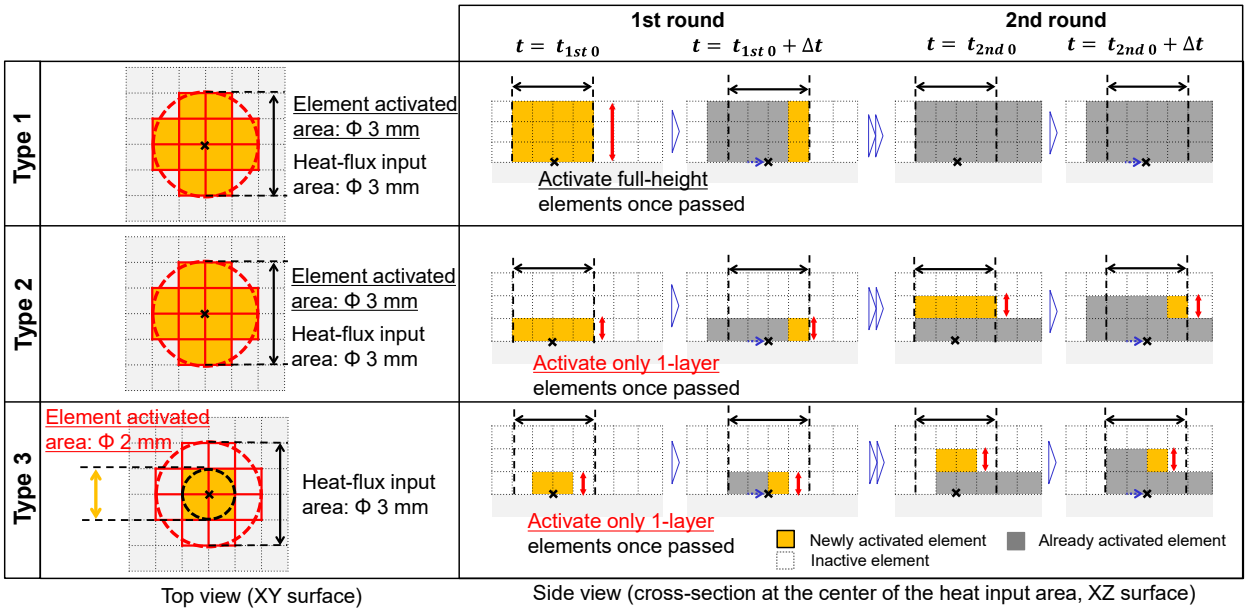

Figure 4 Schematics of the heat-input and element-addition model

At this time, each model was validated for 2 points. The first is a comparison with the experimental maximum temperature on the melt pool surface (1625 , =). The second is a comparison of the base surface temperature to the substrate melting temperature (1400 [22]). **Figure 5** shows the temperature on the surface and the interface with the substrate within the melt

pool diameter at each time. The “Max” value represents the maximum temperature on each surface, and the “Ave Max” value is the average temperature of active nodes adjacent to the node with the maximum temperature. As shown in **Fig.5** (a), (b), the coating surface and base surface temperature in Types 1 and 2 are lower than the experimental result and melting temperature respectively. On the other hand, in Type 3, coating surface and base surface temperatures show a similar temperature with the experimental result and melting temperature, although there is a slight variation. Based on those results, the Type 3 model was selected for the thermal simulation in this study.

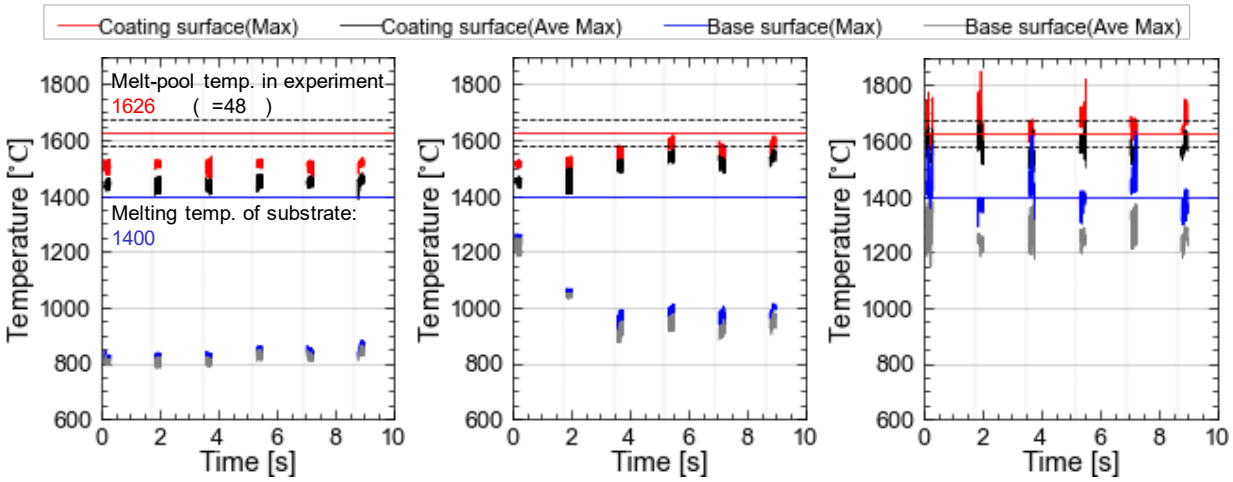

(a) Type 1 (b) Type 2 (3) Type 3

Figure 5 Maximum and spatial averaging maximum temperature of the surface and the interface with the substrate within the melt pool diameter at each time, in (a) Type A, (b) Type B, and (c) Type 3.

2.4. Simulation Conditions

Simulation conditions are summarized in **Table 2**.

Table 2 simulation conditions

Parameter	Unit	Value
Circumference speed	mm/min	5430
Laser rotational speed	min	34.6
Scan speed	mm/min	20
Scan length	mm	10
Laser power	W	2000
Ambient Temperature		25
Heat input time	s	30

In this study, the specific heat and thermal conductivity were temperature-dependent values. To account for latent heat, enthalpy was defined as the integral of the product of specific heat, which considers the latent heat, and density over temperature. The laser absorption rates are defined as 0.37 and 0.5 for the coating layer and workpiece, referencing the preliminary experiments and [23,24].

3. Experimental Method

Coating experiments were conducted using a 5-axis AM system (Lasertec65 3d, DMG MORI CO., LTD), to investigate the effect of workpiece shape and thermal history on the coating properties. Experimental conditions correspond to the simulation. **Figure 6** shows the experimental setups. The cladding material was Ferro55, and its chemical composition is described in **Table 3**. The workpieces were made of SUS304, and the dimensions were 50 mm in diameter and 200 mm in length.

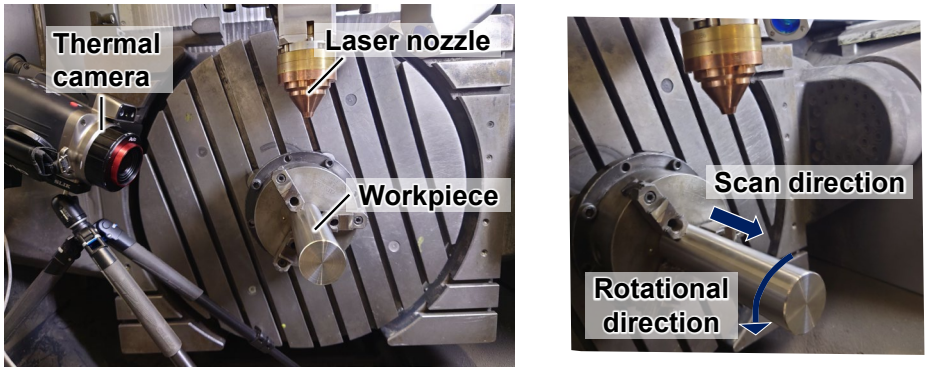

Figure 6 Experimental setup, (left) Overall view, (right) Scan and Rotational directions.

Table 3 Chemical composition of Ferro55 (wt%) [25]

	C	Cr	Mo	Mn	Si	Fe
Content (wt%)	0.35	7.0	2.2	1.1	0.3	balanced

During experiments, the workpiece surface temperature was measured with an infrared thermal camera (InfRec R500 Pro, Nippon Avionics Co.). After experiments, the cross-sections of the coating layer were observed with a digital microscope (VHX-5000 series, KEYENCE Co.) and hardness was measured with a micro-Vickers hardness tester (HM-200Mitutoyo Co.).

4. Result and Discussion

4.1. Thermal History Analysis

As a result of simulations, the temperature distribution with each workpiece was obtained as shown in **Fig.7**.

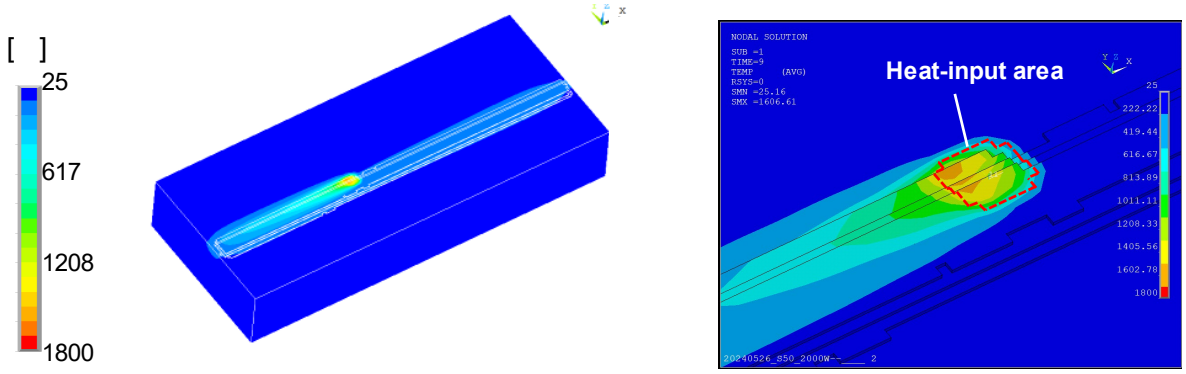

Figure 7 Example of temperature distribution obtained,
(left) Overall view and (right) around the melt pool and heat input area.

Comparison with the experimental result

The maximum temperature on the coating layer surface within the melt pool diameter was compared with those in experiments. **Figure 8** (a) and (b) show the maximum temperature for simulation and experiment. The experimental maximum values were measured in the detection area (**Fig.8** (c)) including the melt pool throughout the process. The lines represent the maximum temperature, and the dots represent the maximum temperature averaged per round. As for the first 10 seconds, the temperature in the experiment was relatively low because the powder supply was unstable during that time as mentioned in the later section. Therefore, the part after 10 s is focused on this time. The difference between the simulation and experimental results was up to 8.4%. However, it cannot be considered as a significant difference in this temperature range, because measuring molten metal is technically difficult, and the measuring data contained noise and high variability.

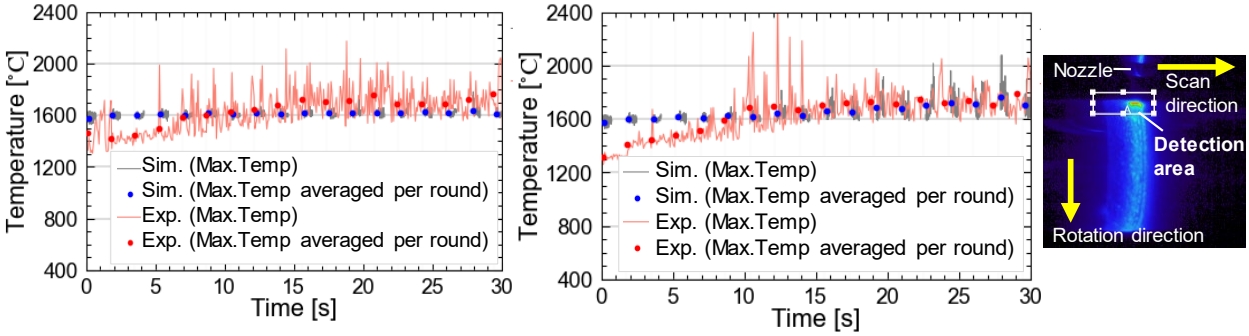

(a) Solid (b) Hollow (c) Detection area

Figure 8 Maximum temperature on the surface for (a) solid and (b) hollow workpieces. (c) Thermal image with the detection area of experimental results.

Comparison of thermal history

To compare the thermal histories, temperature deviation at fixed points was obtained. A total of 24 points were selected as measurement points: 6 points in the workpiece-Y direction (corresponding to the scan direction) on the centerline of the workpiece width (**Fig.9** (a)), and 4 points including the top surface of the coating layer (D = 0.42 mm) and the boundary (D = 0 mm) in the workpiece-Z direction (corresponding to the depth direction) (**Fig.9** (b)).

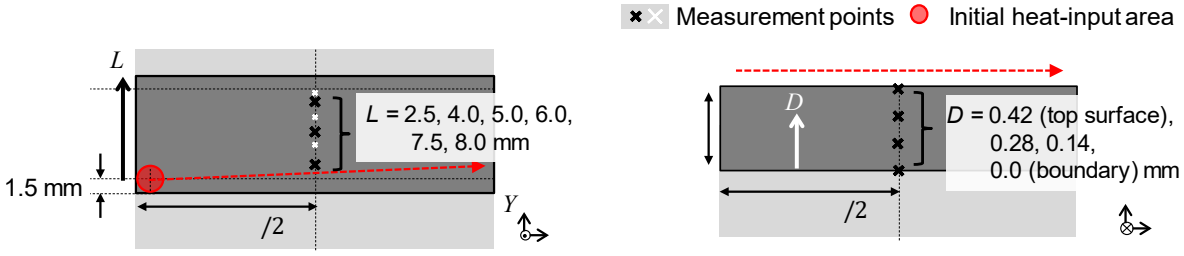

(a) Scan direction (b) Depth direction

Figure 9 Dimensions of measurement points in (a) scan direction and (b) depth direction.

First, **Fig.10** shows a temperature deviation on the top surface (D=0.42 mm). L is the distance in the y-axis from the initial heat input position. As shown in **Fig.10** (a), the peak temperature is observed when the heat-input area passes near the specified point in each round.

The peak temperatures of the hollow condition are slightly higher than those of the solid condition. Comparing the local minimum temperature after each peak temperature for each point of L, it increases as the coating process proceeds in the hollow condition, however, it does not change in the solid condition. **Figure 10** (b) shows that the difference in the local minimum temperature between the solid and hollow increases, and it is 106 near the end of the process (L=7.5 mm). This tendency indicates that the heat accumulates as the coating process proceeds more in the hollow than the solid and would affect the cooling rate, which is related to the hardness of the coating layer.

Next, the cooling rate at the same points is obtained and shown in **Fig.11**. Comparing the peak cooling rate of the solid and hollow conditions, however, there is no significant difference in the range of cooling rates above 100 /s. To investigate the cooling rate in detail, the temperature and cooling rate at the point on the top surface D=0.42 mm, L=7.5 mm for each workpiece condition are compared in **Fig.12**. After each heating, the temperature decreases more quickly in the solid condition than in the hollow condition to temperature (approximately 350 [26,27]), which is the temperature for the start of martensitic transformation, faster. The cooling rates when the temperature reaches after the temperature last exceeds A (approximately 800 [23]) are 2479 /s and 737 /s with the solid and hollow conditions, respectively. Those results suggest that the hardness would be higher in the solid condition than in the hollow condition due to the generation of martensitic structure and suppression of grain coarsening. However, the clacks are likely to increase with the solid because of its higher cooling rate.

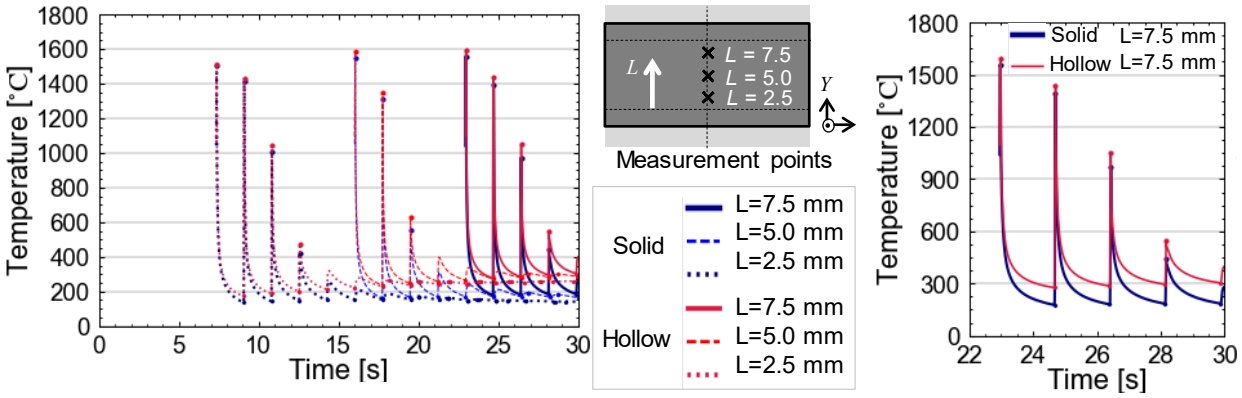

(a) L = 2.5, 5.0, 7.5 mm (b) L = 7.5 mm (22-30 s)

Figure 10 Thermal history (temperature) on the top surface D = 0.42 mm.

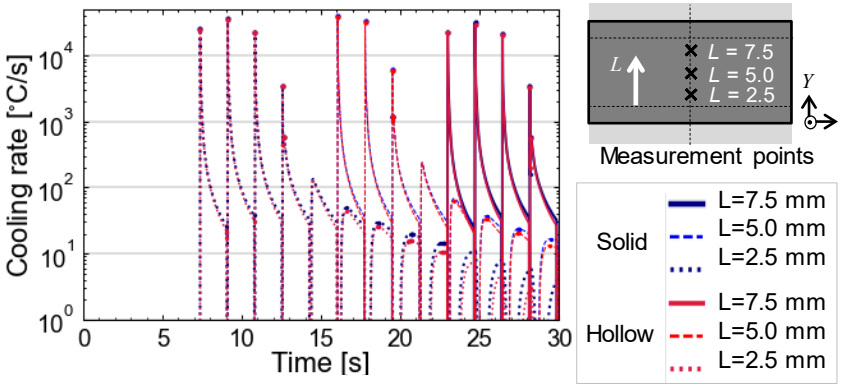

Figure 11 Thermal history (cooling rate) on the top surface D = 0.42 mm.

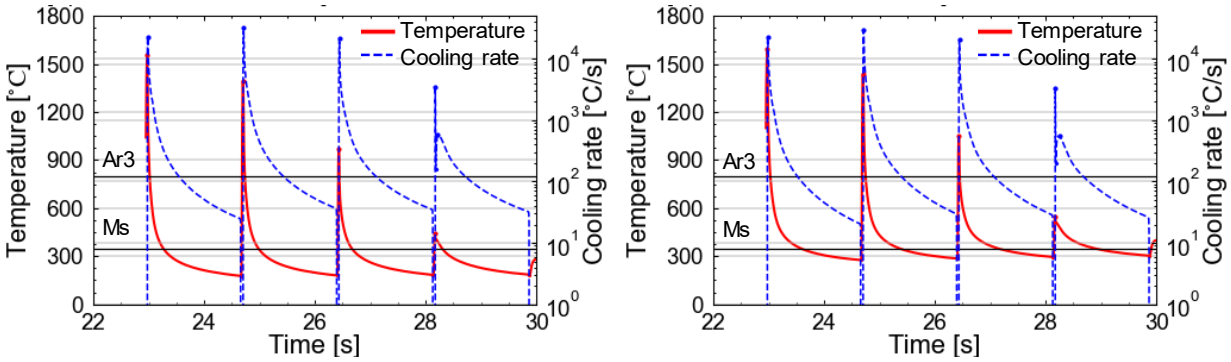

(a) Solid (b) Hollow

Figure 12 Temperature and cooling rate on the top surface D = 0.42 mm, L=7.5 mm (22-30 s), (a) Solid and (b) Hollow.

Figure 13 shows the maximum temperature of the interface with the coating layer and substrate within the melt pool diameter. The meaning and calculation methods of ‘’Max” and “Ave Max” are the same as in **Fig.5**. In both conditions, the maximum temperature is around the melting point of the substrate, although there is a slight variation. It indicates that little penetration would occur in actual coating with these conditions. Additionally, the maximum temperature increases as time progresses in the hollow conditions (**Fig.13** (b)), which is the same tendency as the thermal history of the cladding surface shown in **Fig.10**.

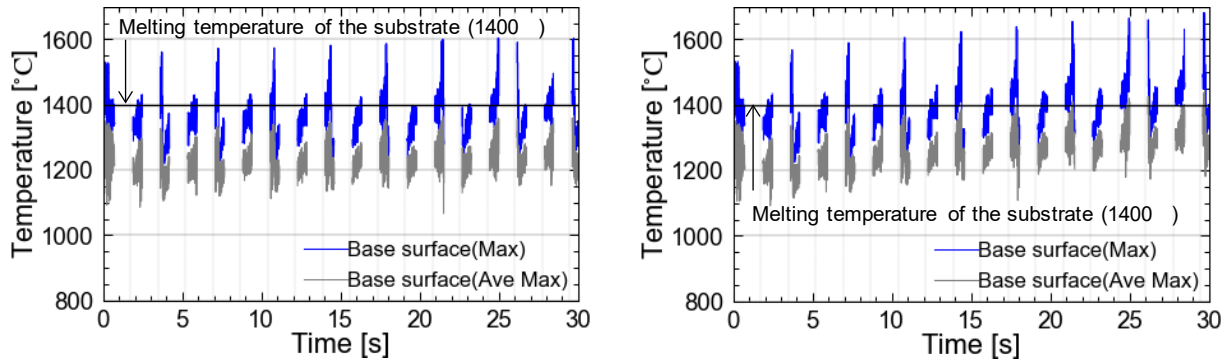

(a) Solid (b) Hollow

Figure 13 Maximum and spatial averaging maximum temperature of the interface with the coating layer and substrate within the melt pool diameter at each time.

4.2. Coating Property Analysis

Figure 14 shows one of the workpieces with coating obtained by experiments. The cross-section of the coating layer along the axis direction, as shown in the figure with the red dotted line, was cut out and polished. For each workpiece, samples were obtained at two diagonal locations on the circumference.

Figure 14 Appearance of the workpiece with coating.

Figure 15 (a), (b) are the cross-sections of the solid workpiece, and (c), (d) are those of the hollow workpiece. The scan direction is right to left in the figures. At first, the heights of the coating layer are lower at the beginning of cladding compared with the subsequent height because of the unstable powder supply. Hence the results of those areas were excluded from further analysis. Comparing the cross-sections of the solid and hollow workpieces, more cracks are observed in samples of the solid workpiece (**Fig.15** (a), (b)) and the difference is more obvious in the latter half of the cladding. This is supposed to be an effect of the faster cooling rate of the solid workpiece as described in Section 4.1 and caused by thermal stress that occurred during solidification.

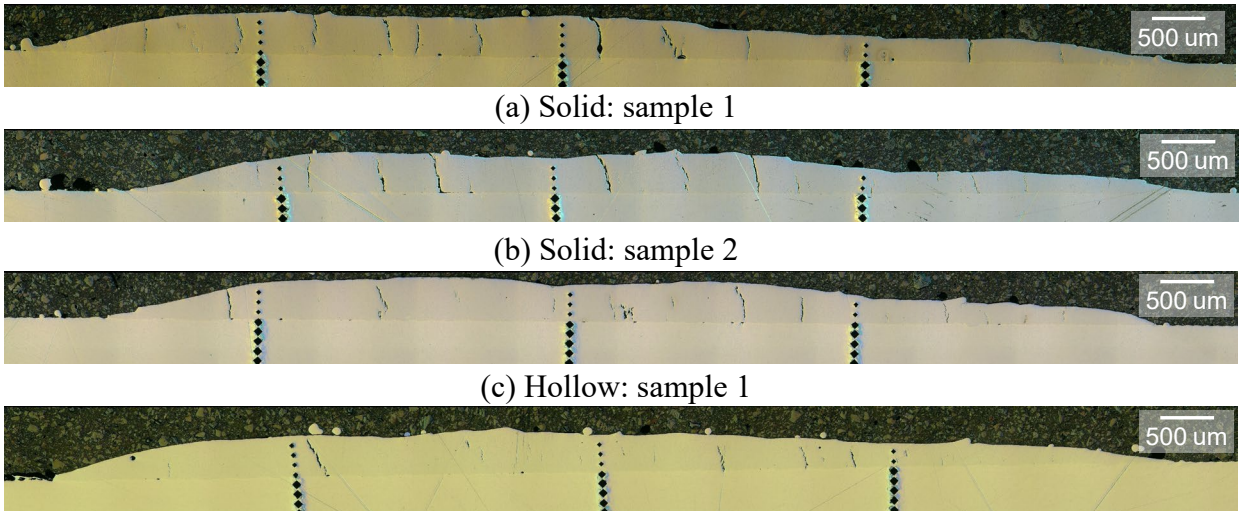

(a) Solid: sample 1

(b) Solid: sample 2

(c) Hollow: sample 1

(d) Hollow: sample 2

Figure 15 Cross-section of the cladding layer of
(a, b) solid workpiece and (c, d) hollow workpiece.

Hardness tests along the depth direction were conducted at three areas around the beginning, middle, and end of the cladding. For the result around the middle and end line, the hardnesses of the cladding layer (**Fig.16** (b)) were averaged for each area (middle and end), and the averaged hardness was summarized in **Fig.16** (a). The error bars represent the maximum and minimum values of each condition. The average hardnesses at the middle and end line of the solid workpiece are 688 HV and 685 HV respectively, and those of the hollow workpiece are 679 HV and 691 HV respectively. These results show no significant difference in hardness even though the cooling rate is higher with the solid condition than with the hollow in the simulation results (**Fig.12**). As a reason for the hardness of the hollow workpiece not decreasing, it is considered that the temperature dropped below the point even if the heat accumulated, and the cooling rate at that time was still sufficiently fast in this coating time range.

These results indicate that the cooling rates of the solid and hollow in this experiment are enough to transform the microstructure into martensite, although there is a difference in cooling rate especially later in the coating. However, as coating time increases further and the temperature does not cross the point as quickly, the hardness is presumed to be affected by differences in cooling rate due to differences in workpieces. On the contrary, the difference is considered to affect the crack generation. In future works, the simulation of metallographic growth should be conducted to reveal the influence of cooling rate and hardness in the high-speed coating in detail. Moreover,

we plan to conduct the thermal stress analysis numerically and experimentally for an even longer coating time.

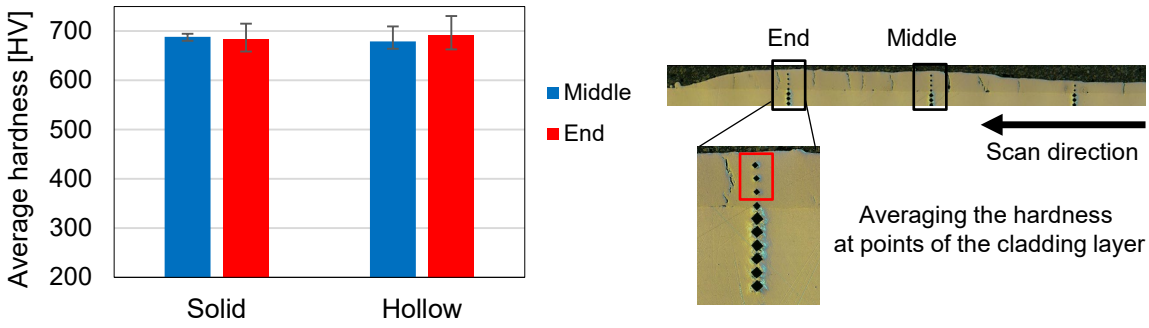

(a) Hardness of the cladding layer (b) Measurement points

Figure 16 Hardness of the solid and hollow workpieces at the points in the cladding layer (b).

5. Conclusion

The effect of workpiece shape on thermal history during high-speed coating using DED was analyzed based on the thermal analysis. Furthermore, the coating experiments were conducted to investigate the effect of workpiece shape and thermal history on the coating properties. The obtained results are summarized as follows:

- The heat-input and element-addition model suitable for high-speed coating using DED was created.

- Comparing the temperature deviation at fixed points, the peak temperature of the hollow condition was slightly higher than that of the solid condition, and the local minimum temperature increased as the coating process proceeded in the hollow condition. Because of those differences, the cooling rates from the time of last crossing to was faster in the solid condition, which was 2479 /s and 737 /s with the solid and hollow conditions, respectively.

- As a result of experiments, there was no significant difference in hardness, however, more cracks were observed in solid results, especially in the latter half of the coating. Those results indicate that the cooling rates of the solid and hollow in this case are enough to transform the microstructure into martensite, however, the difference in cooling rate of the solid and hollow is considered to affect the crack generation.

Acknowledgments

This work was supported by JST SPRING (JPMJSP2123).

References

[1] M. Armstrong, H. Mehrabi, and N. Naveed, “An overview of modern metal additive manufacturing technology,” *Journal of Manufacturing Processes*, vol. 84, pp. 1001–1029, Dec. 2022, doi: 10.1016/j.jmapro.2022.10.060.

[2] *Wohlers Report 2024*. Wohlers Associates, 2024.

[3] D.-G. Ahn, “Directed Energy Deposition (DED) Process: State of the Art,” *Int. J. of Precis. Eng. and Manuf.-Green Tech.*, vol. 8, no. 2, pp. 703–742, Mar. 2021, doi: 10.1007/s40684-020-00302-7.
[4] D. Svetlizky *et al.*, “Directed energy deposition (DED) additive manufacturing: Physical characteristics, defects, challenges and applications,” *Materials Today*, vol. 49, pp. 271–295, Oct. 2021, doi: 10.1016/j.mattod.2021.03.020.
[5] J. C. Heigel, P. Michaleris, and E. W. Reutzel, “Thermo-mechanical model development and validation of directed energy deposition additive manufacturing of Ti–6Al–4V,” *Additive Manufacturing*, vol. 5, pp. 9–19, Jan. 2015, doi: 10.1016/j.addma.2014.10.003.
[6] P. Michaleris, “Modeling metal deposition in heat transfer analyses of additive manufacturing processes,” *Finite Elements in Analysis and Design*, vol. 86, pp. 51–60, Sep. 2014, doi: 10.1016/j.finel.2014.04.003.
[7] G. Zhu, A. Zhang, D. Li, Y. Tang, Z. Tong, and Q. Lu, “Numerical simulation of thermal behavior during laser direct metal deposition,” *Int J Adv Manuf Technol*, vol. 55, no. 9, pp. 945–954, Aug. 2011, doi: 10.1007/s00170-010-3142-0.
[8] T. Mukherjee, W. Zhang, and T. DebRoy, “An improved prediction of residual stresses and distortion in additive manufacturing,” *Computational Materials Science*, vol. 126, pp. 360–372, Jan. 2017, doi: 10.1016/j.commatsci.2016.10.003.
[9] S. Mondal, D. Gwynn, A. Ray, and A. Basak, “Investigation of Melt Pool Geometry Control in Additive Manufacturing Using Hybrid Modeling,” *Metals*, vol. 10, no. 5, Art. no. 5, May 2020, doi: 10.3390/met10050683.
[10] Z. Zhang, P. Farahmand, and R. Kovacevic, “Laser cladding of 420 stainless steel with molybdenum on mild steel A36 by a high power direct diode laser,” *Materials & Design*, vol. 109, pp. 686–699, Nov. 2016, doi: 10.1016/j.matdes.2016.07.114.
[11] H. Lv, Y. Liu, H. Chen, W. Zhang, S. Lv, and D. He, “Temperature field simulation and microstructure evolution of Fe-based coating processed by extreme high-speed laser cladding for re-manufacturing locomotive axle,” *Surface and Coatings Technology*, vol. 464, p. 129529, Jul. 2023, doi: 10.1016/j.surfcoat.2023.129529.
[12] ANSYS, Inc., “Advanced Analysis Guide.” Jan. 2024.
[13] A. Komodromos, J. Grodotzki, F. Kolpak, and A. E. Tekkaya, “Characterization of Tool Surface Properties Generated by Directed Energy Deposition and Subsequent Ball Burnishing,” *Journal of Manufacturing Science and Engineering*, vol. 146, no. 040904, Feb. 2024, doi: 10.1115/1.4063736.
[14] M. Ueda, “CAM-system-based Intelligent Process Planning and Control of Directed Energy Deposition for Easy Fabrication of Accurate Shape,” Thesis for Degree of Ph.D., Keio University, 2020.
[15] J. Goldak, A. Chakravarti, and M. Bibby, “A new finite element model for welding heat sources,” *Metall Trans B*, vol. 15, no. 2, pp. 299–305, Jun. 1984, doi: 10.1007/BF02667333.
[16] C. Baykasoglu, O. Akyildiz, D. Candemir, Q. Yang, and A. C. To, “Predicting Microstructure Evolution During Directed Energy Deposition Additive Manufacturing of Ti-6Al-4V,” *Journal of Manufacturing Science and Engineering*, vol. 140, no. 051003, Feb. 2018, doi: 10.1115/1.4038894.
[17] J. Romano, L. Ladani, and M. Sadowski, “Thermal Modeling of Laser Based Additive Manufacturing Processes within Common Materials,” *Procedia Manufacturing*, vol. 1, pp. 238–250, Jan. 2015, doi: 10.1016/j.promfg.2015.09.012.

[18] S. A. Tsirkas, P. Papanikos, and T. Kermanidis, “Numerical simulation of the laser welding process in butt-joint specimens,” *Journal of Materials Processing Technology*, vol. 134, no. 1, pp. 59–69, Mar. 2003, doi: 10.1016/S0924-0136(02)00921-4.
[19] M. I. Al Hamahmy and I. Deiab, “Review and analysis of heat source models for additive manufacturing,” *Int J Adv Manuf Technol*, vol. 106, no. 3–4, pp. 1223–1238, Jan. 2020, doi: 10.1007/s00170-019-04371-0.
[20] H. Liu, M. Li, X. Qin, S. Huang, and F. Hong, “Numerical simulation and experimental analysis of wide-beam laser cladding,” *Int J Adv Manuf Technol*, vol. 100, no. 1, pp. 237–249, Jan. 2019, doi: 10.1007/s00170-018-2740-0.
[21] L. Costa, R. Vilar, T. Reti, and A. M. Deus, “Rapid tooling by laser powder deposition: Process simulation using finite element analysis,” *Acta Materialia*, vol. 53, no. 14, pp. 3987–3999, Aug. 2005, doi: 10.1016/j.actamat.2005.05.003.
[22] “MatWeb - The Online Materials Information Resource.” Accessed: Jun. 11, 2024. [Online]. Available: https://www.matweb.com/search/QuickText.aspx
[23] S. Oh and H. Ki, “Prediction of hardness and deformation using a 3-D thermal analysis in laser hardening of AISI H13 tool steel,” *Applied Thermal Engineering*, vol. 121, pp. 951–962, Jul. 2017, doi: 10.1016/j.applthermaleng.2017.04.156.
[24] A. Hozoorbakhsh, M. I. S. Ismail, A. A. D. M. Sarhan, A. Bahadoran, and N. B. A. Aziz, “An investigation of heat transfer and fluid flow on laser micro-welding upon the thin stainless steel sheet (SUS304) using computational fluid dynamics (CFD),” *International Communications in Heat and Mass Transfer*, vol. 75, pp. 328–340, Jul. 2016, doi: 10.1016/j.icheatmasstransfer.2016.05.008.
[25] “Metal Powders - voestalpine Böhler Welding.” Accessed: Jun. 10, 2024. [Online]. Available: https://www.voestalpine.com/welding/global-en/products/product-search/metal-powders/
[26] K. Zhang, S. Dai, B. Jiang, X. Zheng, J. Liu, and X. Zhang, “Feasibility Study for the Remanufacturing of H13 Steel Heat-Treated TBM Disc Cutter Rings with Uniform Wear Failure Using GMAW,” *Materials*, vol. 16, no. 3, Art. no. 3, Jan. 2023, doi: 10.3390/ma16031093.
[27] Oerlikon Metco, “Material Product Data Sheet H13 Hot Work Tool Steel Powder for Additive Manufacturing.”